Heritage Science

RESEARCH

Open Access

Investigating the effect of nanolime treatment on the drying kinetics of Clipsham limestone

Dáire E. Browne[1,2], Robert Peverall[1], Grant A. D. Ritchie[1*] and Heather A. Viles[2]

Abstract

Climate change poses an ever-increasing risk to our stone built heritage. Among conservation actions, the use of consolidant products is considered a possible response to this challenge, and the adoption of nanolimes has been widely studied showing promising results. However, while the effectiveness and method of application has been assessed, few studies have probed the changes in drying kinetics following treatment. In fact, a drastic alteration of the water transport might lead to further anomalies. This study investigates the influence of nanolimes dispersed in ethanol on the drying kinetics of Clipsham limestone using cavity ring-down spectroscopy. The degree of treatment was assessed by gravimetry, Raman spectroscopy, optical microscopy, colorimetry, optical profilometry and thin section analysis. Results showed an increase in the dry mass, observable colour changes and decrease in surface roughness. Small but reproducible increases were observed in the evaporation flux for phase I behaviour following treatment, however, no changes were observed in the total mass of water released or the phase II diffusivity. Determination of the activation energy associated with phase II drying was unchanged following treatment . These results indicate that following treatment there has been little-to-no change in the internal surfaces and structure of the stone to affect vapour transport.

Keywords Cavity ring-down spectroscopy, Limestone, Drying kinetics, Consolidant

Introduction

The deterioration and conservation of stone built heritage is a significant area of research, especially due to increasing threats which accompany climate change. Deterioration of the stone can result in the loss of cohesion, leading to powdering, flaking, blistering and other forms of material loss. Therefore, it is often necessary to apply a consolidant to restore strength and provide resistance to various damage mechanisms [1]. An ideal consolidant must be compatible with the substrate, have high durability and offer retreatability [2]. Therefore, it is unsurprising that finding a suitable consolidant can be extremely difficult, and a variety of materials have been tried.

For the consolidation of limestone, inorganic lime-based consolidants should be preferably considered. Traditionally, limewater (an aqueous suspension of $Ca(OH)_2$) was widely used due to its compatibility with the substrate and high durability [2]. Consolidation of limestone occurs via the carbonation reaction of $Ca(OH)_2$ in the presence of CO_2 resulting in the formation of $CaCO_3$ [3], the main component of the limestone matrix. However, due to the limited solubility of $Ca(OH)_2$ in water (1.65 g/L at 20 °C [4]), large quantities of aqueous solution are required to achieve consolidation, and this poses other risks such as that of freeze–thaw weathering or salt

*Correspondence:
Grant A. D. Ritchie
grant.ritchie@chem.ox.ac.uk
[1] Department of Chemistry, University of Oxford, South Parks Road, Oxford OX1 3QZ, UK
[2] School of Geography and the Environment, University of Oxford, South Parks Road, Oxford OX1 3QY, UK

migration [5]. Another drawback is the limited penetration depth of limewater, with the majority of the lime depositing near the surface and in some cases forming a white film that can be seen following application [2, 6].

The use of nanolimes—dispersions of nanometre sized $Ca(OH)_2$ crystals—was proposed by Giorgi et al. [6] in 2000 in order to address these limitations. In their study, Giorgi et al. [6] compared the kinetic stability of $Ca(OH)_2$ dispersed in water versus propan-1-ol, and found that the alcohol dispersion had higher kinetic stability. The use of alcohol dispersions also offers the advantages of limiting carbonation of the nanolimes particles by CO_2 before they have been deposited in the stone [2, 4], and allowing a higher concentration of $Ca(OH)_2$, e.g., commercial nanolime *CaLoSiL* (IBZ-Salzchemie GmbH & Co, Germany) is available in concentrations of 50 g/L. However, it is important to note that the use of alcohol dispersions requires appropriate health and safety precautions to carefully control the risk to the user and the environment [4].

Since then, nanolimes have been widely studied [4, 7] and the literature can broadly be divided into two main groups: the first group concerns the study of the nanolimes themselves, determining the mechanism of the carbonation process [8–11] as well as improving the efficacy and synthesis of nanolime [12–16]. The second group mostly focuses on the application of these nanolimes to different substrates [1, 17–25], in various environmental conditions [5, 26, 27] and with different application procedures [28–32]. Within this second group, the compatibility and effectiveness of the nanolime treatment have been assessed in terms of penetration depth, strength, hardness, surface cohesion, capillary absorption and aesthetics. However, few studies have investigated the impact of nanolime treatment on the water drying kinetics despite reports of a decrease in measured porosity and accumulation of nanolimes near the surface [3, 21, 33–35]. If this accumulation alters the water transport kinetics, and as the consolidation treatment is irreversible, this will result in a permanent and dramatic change which may result in trapped moisture leading to increased weathering [3].

Recently, we have developed and reported on the use of near-infrared continuous-wave (cw) cavity ring-down spectroscopy (CRDS) to monitor the release of water from small (*ca.* $25 \times 25 \times 5$ mm) samples of Clipsham limestone [36] and a follow-up study demonstrating the universality of the technique when applied to different stone samples [37]. In these experiments, the drying kinetics showed the expected two phase drying behaviour for porous materials which consists of an initial constant drying rate period (phase I) followed by a falling drying rate period (phase II) [38, 39]. During phase I, the rate of evaporation is controlled by the concentration gradient between the surface and the gas above. The pores at the surface are supplied by water by flow through connected pathways, and the gas at the surface is fully saturated leading to a constant rate of evaporation. As the drying proceeds further, disconnected pathways begin to form within the material, decreasing the surface water content and resulting in the gas at the surface becoming unsaturated. Eventually, the unsaturated capillary flow is no longer sufficient to maintain a constant rate of evaporation and phase II drying begins. Vapour transport through the material now dominates, and is controlled by the internal structure and properties of the material.

We have also demonstrated that, using this technique, the influence of temperature on the drying kinetics can be investigated [37]. We have shown that the phase II diffusivity increases with temperature, allowing determination of an activation energy which characterises the surface interactions that occur during the diffusion of water through the porous stone. We have previously determined that for Clipsham limestone the activation energy for phase II diffusivity is 31.87 ± 1.79 kJ mol^{-1} [37], which is lower than the enthalpy of vaporisation from liquid water. Previous research has suggested that this decrease could be due to varying surface roughness [40].

The aim of this study is to use this highly sensitive technique to study the influence of ethanol dispersed nanolime treatments on the drying kinetics of Clipsham limestone. Studies are conducted at a variety of temperatures to determine if treatment has an impact on the phase II activation energy. The degree of treatment is assessed by gravimetry, Raman spectroscopy, optical microscopy, colorimetry, optical profilometry and thin section analysis.

Materials and methods

Stone type: Clipsham limestone

This work focuses on the treatment of Clipsham limestone, a commonly used construction [41] and repair [42, 43] stone. It is a coarse grained ooidal and shell fragmental grainstone with occasional herringbone cross-bedding (Fig. 1a, C0), originating from the Lincolnshire Limestone Formation (Middle Jurassic, Bajocian) [44, 45]. It has a broad unimodal pore size distribution with a open porosity of 20.16 % and peak pore diameter of 0.84 μm, as shown in Fig. 1b. A full characterisation of this limestone can be found in our previous research [36, 37].

Previous research on different limestones, such as Maastricht [1, 33, 46, 47], Lecce [18], Doulting [31] and Migné [47], has reported that treatment with alcohol dispersed nanolimes results in limited penetration, and due to back-migration of the nanoparticles during solvent

evaporation, the nanolime is mostly found at distances less than 1 cm from the drying face [4, 32]. To ensure full treatment of the sample, as well as allow relatively fast drying experiments, the dimensions of the sample were cut to *ca.* 25 × 25 × 5 mm; eight replicate samples were investigated.

Consolidant and application procedure

The influence of treatment on the drying kinetics was investigated at two different concentrations. Commercially available nanolime *CaLoSiL E25* (IBZ-Salzchemie GmbH & Co, Germany) was selected due to its prevalence in nanolime research [10, 12, 16, 17, 20, 21, 30]. *CaLoSiL E25* (*E25* hereinafter) is a colloidal dispersion of $Ca(OH)_2$ nanoparticles in ethanol at a concentration of 25 g/L, with a particle size distribution reported between 50 and 300 nm, as shown in Fig. 1b, which is in agreement with literature values [48, 49]. The applied suspension was well within its shelf-life and the ethanol solvent is known to promote kinetic stability [9, 46, 47]. However, general consensus and advice for conservation practice promotes initially using lower concentrations of alcohol dispersed nanolimes (e.g., 5 or 10 g/L), in order to prevent the formation of a white haze and improve penetration into the sample [4, 29, 50]. Therefore, a second concentration of 5 g/L (*E5* hereinafter) was obtained by diluting one part *E25* with four parts ethanol (Sigma Aldrich, p.a. > 99.8 %). To mitigate the Ca-alkoxide conversion, the nanolimes were stored in a refrigerator ($T \approx 5$ °C) before and between treatments [9, 10, 31].

Samples were treated by full immersion, and weighed in 5 min intervals using a KERN PLS 420–3F mass balance (max. 420 g, $\delta = 0.001$ g). The samples were wiped with a solvent dampened cloth to remove excess consolidant and prevent whitening [17, 21, 31, 34]. The treatment was carried out for a total period of 60 min to ensure saturation of the sample was achieved, i.e., when the weight of the sample reached a constant value. The procedure was repeated every 24 h when the samples were dry, for a total period of 5 days. Following this, to ensure carbonation of the nanolimes, the samples were stored in an environmental chamber (Binder KBF 115) at $T = 20$ °C, % $RH = 75$ for 28 days [4, 9, 26, 29, 48]. Four samples were treated at each concentration to investigate reproducibility.

Characterisation of consolidants and their impacts

To assess application and carbonation of the treatment, Raman spectra were taken in the range 50 – 1500 cm^{-1} using a Thermo Scientific DXR3 SmartRaman spectrometer at 785 nm. The laser output power was 5 mW with a spot size of 3.1 μm. Raman spectra were taken weekly during the carbonation period and each spectrum was taken from an average of 500 scans with a resolution of 2.3 cm^{-1}.

Optical microscopy was performed using a Dino-Lite Edge (AM7915MZT) digital microscope to evaluate the surface of the material and observe the presence of deposits. Colorimetric measurements were carried out using a Konica Minolta CM-700d spectrophotometer, using a D65 illuminant, 10° observer angle, and a 3 mm spot diameter. Measurements were taken on both the top and bottom surface of the samples, with 20 measurements per face. The aesthetic changes were determined using CIELAB colour space [51] and the global colour change was calculated using:

$$\Delta E^*_{ab} = \sqrt{\Delta L^* + \Delta a^* + \Delta b^*} \quad (1)$$

where ΔL^* is the change in lightness, Δa^* is associated with changes in red–green hues and Δb^* is associated with changes in blue–yellow hues compared with a control (untreated) sample group.

Surface roughness measurements were taken on the top and bottom face of the samples following the 28 day curing period and compared with the surface roughness for control samples, measured using the same method, to assess the accumulation of the nanolime product. The changes in surface roughness were measured using an Innowep TRACEiT optical profilometer, which creates a 3D-topographical map of the surface. Measurements are taken over a 5 × 5 mm area, with a resolution of 3 μm horizontally (*xy*-axes) and 1.5 μm vertically (*z*-axis) [52]. An average of 1536 transects in the *x*- and *y*-axes are used to determine the arithmetic average height parameter, R_a, across the measuring area [53].

To examine the stone petrology, thin sections of a control sample, *E5* sample and *E25* sample were prepared according to BS EN 12407:2007 [54] to 30 μm thickness and protected with a slide cover. The samples were impregnated with resin to prevent disintegration and dyed blue to help discriminate pores from the stone matrix. Samples were characterised using polarised light microscopy using an Olympus BX43 microscope with LED light source equipped with Olympus SC50 camera. In addition, scanning electron microscopy images of exemplar control and treated samples were obtained using a scanning electron microscope (JEOL JSM6010). The samples were sputter coated with carbon. These images are provided in the Additional file 1.

Cavity ring-down spectroscopy

Molecules absorb light at different frequencies due to their unique sets of quantum mechanical energy levels. Therefore, a molecule of interest can be selectively excited by choosing light at a specific frequency and its

concentration can be quantified by measuring the attenuation in light intensity after said radiation has passed through the absorbing sample. The Beer–Lambert law, $I_{tr} = I_0 \exp[-\alpha(\nu)d]$, gives the relationship between the initial light intensity, I_0, and the transmitted light intensity, I_{tr}, at frequency ν, where $\alpha(\nu)$ is the absorption coefficient and d is the path length over which the light is absorbed. The absorption coefficient is related to the number density, N, by $\alpha(\nu) = N\sigma(\nu)$, where $\sigma(\nu)$ is the species dependent absorption cross-section. Therefore, absolute number densities can be determined by absorption measurements.

Increasing the path length, d, over which the light interacts with the sample allows smaller values of $\alpha(\nu)$ to be measured, and therefore, increases the sensitivity of the absorption measurement. Cavity ring-down spectroscopy (CRDS) achieves this increase in path length by trapping the light between two highly reflective mirrors (the cavity) [55–59] and monitoring the light intensity leaking out of the cavity (after the light has been switched off; or the cavity is no longer illuminated). The time taken for the intensity to fall to $1/e$ of its original value is recorded, and is known as the ring-down time, τ_0. In the presence of an absorbing species, the rate of decay is faster as there is an additional loss mechanism, and the decay time is reduced, resulting in a different ring-down time, τ. The absorption coefficient can be determined from the difference in the reciprocals of the ring-down times:

$$\alpha(\nu) = \frac{1}{c}\left(\frac{1}{\tau} - \frac{1}{\tau_0}\right) \tag{2}$$

where c is the speed of light, and thus, allows the number density of the species of interest to be determined.

A schematic of the near-IR CRDS instrument used in this work is shown in Fig. 2, and a full description of the theory and instrument can be found in Browne et al. [36]. The optical cavity is formed using two highly reflective mirrors (Layertec, $R \approx 0.9999$, radius of curvature = 1 m), placed 86 cm apart. The cavity is excited using a continuous wave (cw) fibre-coupled distributed feedback diode laser (NTT Electronics NLK1S5GAAA, $\lambda = 1506$ nm). A temperature controlled (range = 10 − 50 °C, $\delta = 0.1$ °C) insulated stainless steel chamber (13 × 7 × 8 cm), which is separated from the cavity by a valve, is used to control the environment the stone samples are tested under. The experiments were carried out in a N_2 (BOC Oxygen Free Nitrogen, 99.998 %) gas flow, controlled with calibrated mass flow controllers (MKS 1479A Mass-Flo and MKS PR4000B-S).

The same experimental procedure described in Browne et al. [36, 37] is used. Briefly, for the reproducibility measurements, the sample chamber is set to 25 °C (determined using a calibrated thermocouple) and left undisturbed for 30 min to ensure equilibrium is reached. The samples are immersed in distilled water for 2 days to ensure they are fully saturated, and their wet mass, m_w, is recorded before being placed in the sample chamber. The valve to the main cavity is opened and a constant flow of 1.5 standard litres per minute (slm) dry N_2 is passed over the sample (gas velocity $\simeq 7 \times 10^{-3}$ m s^{-1}). The laser is tuned to the centre of the H_2O $10,3,7(021) \leftarrow 11,3,8(000)$ transition at 6638.91 cm^{-1} [60] and the average ring-down time (RDT) of ten ring-down events is continuously measured. The procedure is stopped when the measured RDT returns to τ_0 and the dry mass of the sample, m_d, is then recorded. Measurements were taken before and after treatment and the 28 day curing period to allow the changes in drying kinetics to be fully probed. For the investigation into the influence of temperature, the temperature of the sample chamber is changed from 20 − 40 °C in 5 °C steps, and the rest of the procedure remains the same.

Analysis of the drying kinetics

A complete description of the analysis can be found in Browne et al. [36]. Following the procedure described above, the time-dependent release of water can be determined from the measured ring-down times. Using Eq. 2, the absorption coefficient, $\alpha(\nu)$, is calculated and from this, the concentration, N, can be determined using $\alpha(\nu) = N\sigma(\nu)$. The concentration is related to the mass of water released from the sample by:

$$m_{H_2O}(t) = \frac{fM_r}{N_A}\int_0^t N\,dt \tag{3}$$

where f is the volumetric flow rate, $M_r(H_2O) = 0.018$ kg mol^{-1} and N_A is Avogadro's number. The normalised mass difference, Δm_n, is defined as:

$$\Delta m_n = \frac{m_{H_2O}(\infty) - m_{H_2O}(t)}{m_d} \tag{4}$$

while the mass flux, $\dot{m}(t)$ is calculated by:

$$\dot{m}(t) = \frac{1}{A}\frac{dm_{H_2O}(t)}{dt} \tag{5}$$

where A is the surface area of the top face of the sample. The time at which phase I ends is denoted as the critical time, t_c, and is determined as the intercept between two tangents fitted to phase I and II time periods in $\dot{m}(t)$. This is achieved via an iterative procedure, in which the intercept is set as the upper limit for the phase I linear fit, and the process repeated until a constant t_c results. An initial period in which the stone sample comes into equilibrium with the environmental chamber is observed in the mass flux, and this period (approximately 10 min) is excluded

Table 1 Characterisation of treatment with *E5* and *E25* for different samples C1–C8

	Sample	Δm_d / g	$\frac{\Delta m_d}{V}$ / kg m^{-3}	ΔL^*	Δa^*	Δb^*	ΔE^*_{ab}	R_a / μm
E5	C1	−0.001±0.001	−0.45±0.45	1.71 ± 2.33 0.52 ± 2.24	−0.62 ± 0.82 −0.43 ± 0.83	1.25 ± 2.69 1.70 ± 2.60	2.21 ± 2.37 1.81 ± 2.54	2.63 ± 0.29 2.30 ± 0.17
	C2	0.008±0.001	2.39±0.30	2.40 ± 2.35 2.61 ± 2.41	−0.48 ± 0.78 −0.43 ± 0.84	−2.06 ± 2.27 −1.90 ± 2.65	3.20 ± 2.29 3.25 ± 2.48	2.78 ± 0.14 2.61 ± 0.06
	C3	0.002±0.001	0.62±0.31	5.07 ± 2.28 4.93 ± 2.43	−1.25 ± 0.77 −1.20 ± 0.73	−4.40 ± 2.34 −4.09 ± 2.35	6.83 ± 2.27 6.52 ± 2.36	2.28 ± 0.05 1.83 ± 0.11
	C4	−0.001±0.001	−0.28±0.28	0.18 ± 2.48 1.47 ± 2.28	−0.49 ± 0.88 −0.72 ± 0.91	−4.25 ± 2.71 −4.26 ± 2.66	4.28 ± 2.70 4.56 ± 2.59	2.21 ± 0.06 1.88 ± 0.08
E25	C5	0.006±0.001	2.56±0.43	2.75 ± 2.19 1.51 ± 2.42	−0.99 ± 0.79 −0.77 ± 0.83	−1.27 ± 2.55 −0.95 ± 2.47	3.19 ± 2.16 1.94 ± 2.26	2.64 ± 0.16 3.25 ± 0.29
	C6	0.010±0.001	2.92±0.29	4.87 ± 3.96 5.35 ± 2.42	−1.21 ± 1.09 −1.11 ± 0.83	−4.89 ± 2.55 −4.90 ± 2.47	7.00 ± 3.45 7.34 ± 2.26	1.97 ± 0.09 2.41 ± 0.08
	C7	0.017±0.001	4.88±0.29	7.38 ± 3.11 6.23 ± 3.07	−1.76 ± 0.82 −1.60 ± 0.86	−5.95 ± 2.44 −5.41 ± 2.48	9.64 ± 2.82 8.40 ± 2.78	2.60 ± 0.14 1.86 ± 0.01
	C8	0.032±0.001	8.27±0.26	11.70 ± 2.28 11.67 ± 2.34	−2.87 ± 0.76 −2.85 ± 0.81	−12.93 ± 2.21 −12.87 ± 2.29	17.67 ± 2.21 17.60 ± 2.29	1.67 ± 0.03 1.26 ± 0.21

Δm_d: dry mass difference; $\frac{\Delta m_d}{V}$: mass difference per unit volume; ΔL^*: change in lightness; Δa^*: change in red–green hues; Δb^*: change in blue–yellow hues; ΔE^*_{ab}: global colour change calculated using equation 1; R_a:mean surface roughness

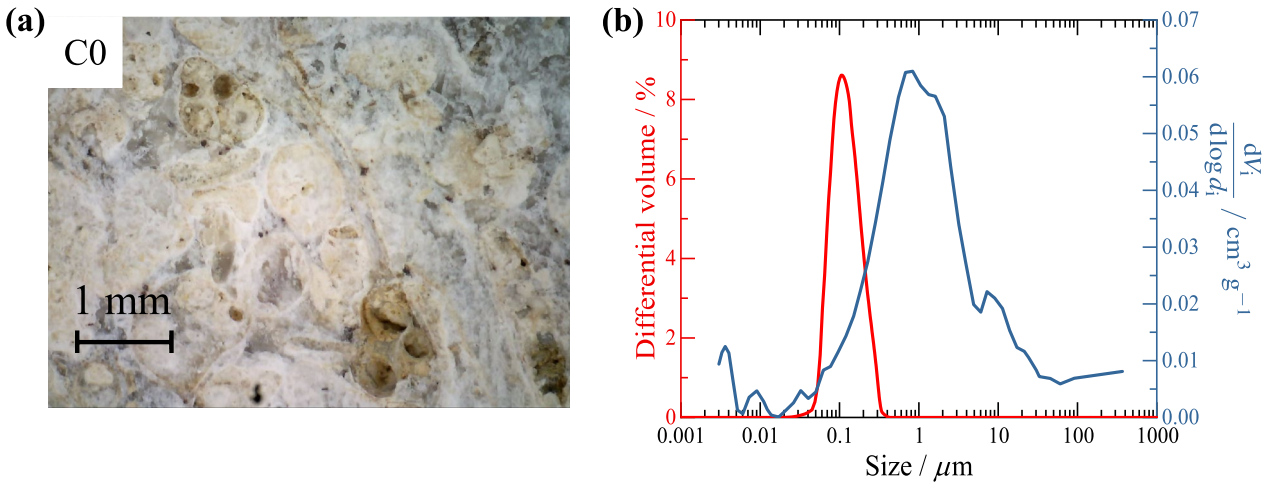

Fig. 1 **a** Optical microphotograph for a control sample (C0); **b** Left hand axis (red): Particle size distribution of *CaLoSiL E25* (IBZ-Salzchemie GmbH & Co, Germany), provided by the manufacturer; Right hand axis (blue): Pore size distribution for Clipsham limestone, obtained by mercury intrusion porosimetry by the British Geological Survey

in the determination of the critical time and the constant mass flux, $\dot{m}_{\mathrm{CST}}$.

In phase II, the capillary flow is insufficient to maintain the constant rate of evaporation found in phase I, and the dominant transport mechanism occurs via vapour transport. Thus, the drying in this phase can be characterised by a diffusivity parameter, D_{II}, which originates from Fick's second law, $(\partial C/\partial t) = D_{\mathrm{II}}(\partial C/\partial x)$. Assuming a uniform distribution of moisture through the porous sample, and integrating over the sample thickness, L, results in the following solution [61]:

$$\frac{m_{\mathrm{H_2O}}(t)}{m_{\mathrm{H_2O}}(\infty)} = 1 - \sum_{n=0}^{\infty} \frac{8}{(2n+1)^2\pi^2} \exp\left\{\frac{-D_{\mathrm{II}}(2n+1)^2\pi^2 t}{4L^2}\right\} \tag{6}$$

When the sample has entered the later stages of drying, and the moisture content has fallen below 40 %, only the first term of Eq. 6 needs to be considered [62], and D_{II} can be determined from the following linear relationship:

$$\ln\left(1 - \frac{m_{\mathrm{H_2O}}(t)}{m_{\mathrm{H_2O}}(\infty)}\right) - \ln\left(\frac{8}{\pi^2}\right) = -\frac{D_{\mathrm{II}}\pi^2 t}{4L^2} \tag{7}$$

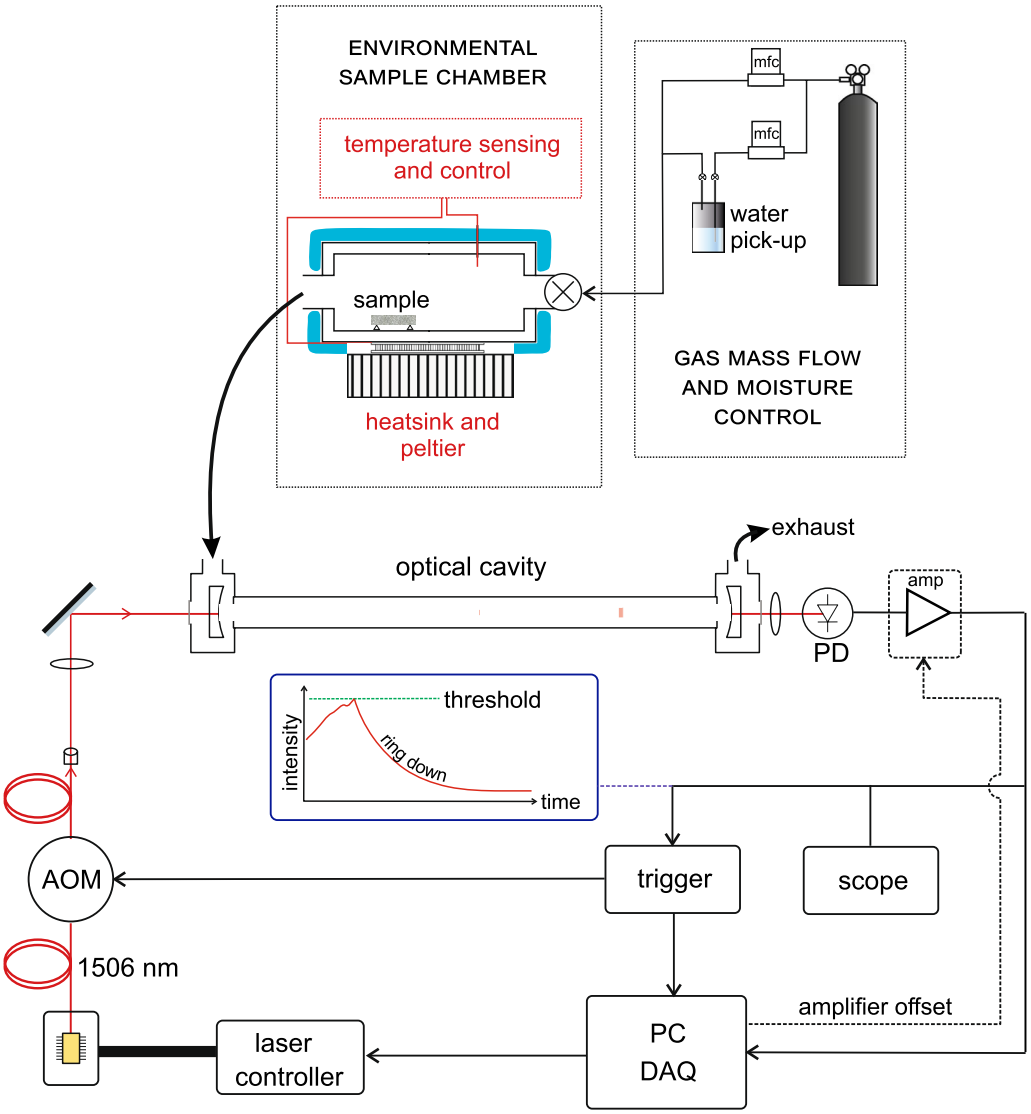

Fig. 2 A depiction of the experimental set-up used to measure H_2O released from limestone. The sample is placed in a temperature controlled cell separate from the cavity ring-down spectrometer. *mfc* mass flow controller; *AOM* acousto-optic modulator; *PD* photo-detector; *amp* amplifier; *PC DAQ* data acquisition system

To ensure that only the first term of Eq. 6 applies, the linear fit for D_{II} is taken between 10–30 % saturation.

As previously stated, the phase II diffusivity increases with temperature and can be characterised by an activation energy, E_a, assuming an Arrhenius type relationship:

$$\ln D_{\mathrm{II}}(T) = \ln D_0 - \frac{E_a}{RT} \tag{8}$$

where D_0 is a temperature-independent pre-exponential factor, R is the gas constant and T the absolute temperature. Thus, the activation energy, E_a can be determined from the gradient of a linear fit of $\ln(D_{\mathrm{II}})$ against $1/T$.

Results and discussion

Characterisation of the treatment

The amount of nanolime absorbed by each sample as a result of treatment has been estimated as the difference in dry mass (Δm_d) before and after the 28 day curing period at $T = 20$ °C and 75 % *RH*. The results for the different samples are reported in Table 1, and in general show that although there was clear absorption of the consolidant, a change in dry mass of a few tens of mg at most is observed (1–10 mg is typical) which is of similar magnitude to that reported by others [21, 31, 33]. As expected, the samples treated with *E25* show a larger Δm_d in comparison to those treated with *E5* due to the higher

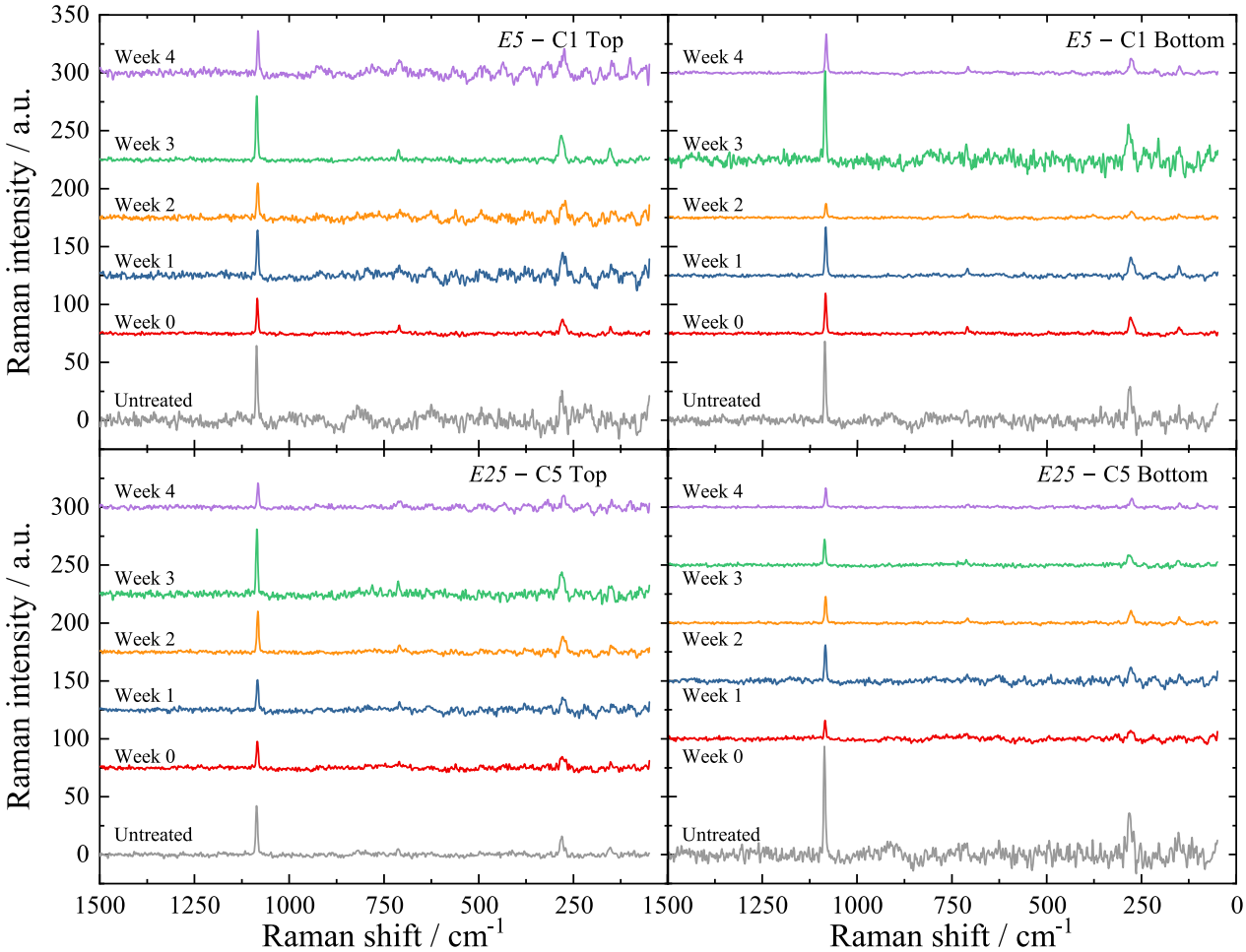

Fig. 3 Raman spectra of the top and bottom limestone surface untreated and treated with *E5* (C1) and *E25* (C5), following each week of curing at *T* = 20 °C, % *RH* = 75

concentration of $Ca(OH)_2$ present in the *E25*. Assuming complete conversion of $Ca(OH)_2$ to $CaCO_3$, the Δm_d values observed would be equivalent to a few monolayers of $CaCO_3$ and therefore, would not be expected to have resulted in large changes in the internal pore structure.

As stated previously, Raman spectra were taken weekly during the carbonation period, and the results are shown in Fig. 3. The Raman spectra show the presence of $CaCO_3$ bands at 1088 cm^{-1} (symmetric stretching vibration $\nu_1[CO_3^{2-}]$), 711 cm^{-1} (in-plane bending vibrations $\nu_4[CO_3^{2-}]$), 281 cm^{-1} (Ca–O lattice vibrations) and 154 cm^{-1} (Ca–O lattice vibrations) [63], but do not show the initial presence of the $Ca(OH)_2$ band at 359 cm^{-1} (Ca–O lattice vibrations) and its subsequent decrease, e.g., as reported by Becerra et al. [35]. We note, however, that Becerra et al. [35] investigated $Ca(OH)_2$ nanoparticles doped with ZnO quantum dots, which may have an influence on the efficacy of the Raman scattering measured. From the Raman spectra we measured, there is no evidence of consolidant on the surface, and thus, we are unable to use this to evaluate the extent of the carbonation process.

Figure 4a shows the optical microphotographs for a control sample (C0), the samples treated with *E5* (C1–C4) and those treated with *E25* (C5–C8) following the carbonation process. From Fig. 4a, deposits of consolidant on the surface can be seen and visual observations confirm whitening of the samples following application, with a greater change observed for the *E25* samples.

Examination of the thin section microphotographs shown in Fig. 4b shows that there is no distinguishable difference between the control, *E5* sample and *E25* sample. A similar conclusion holds for the SEM images (see Additional file 1: Fig. S1). All samples consist of a sparite matrix containing micrite ooids and bioclasts with a calcite rind. The samples show that porosity is formed both in the ooids and the matrix. It is unsurprising that the nanolime deposits are unable to be distinguished in the thin sections as the average size of the nanoparticles

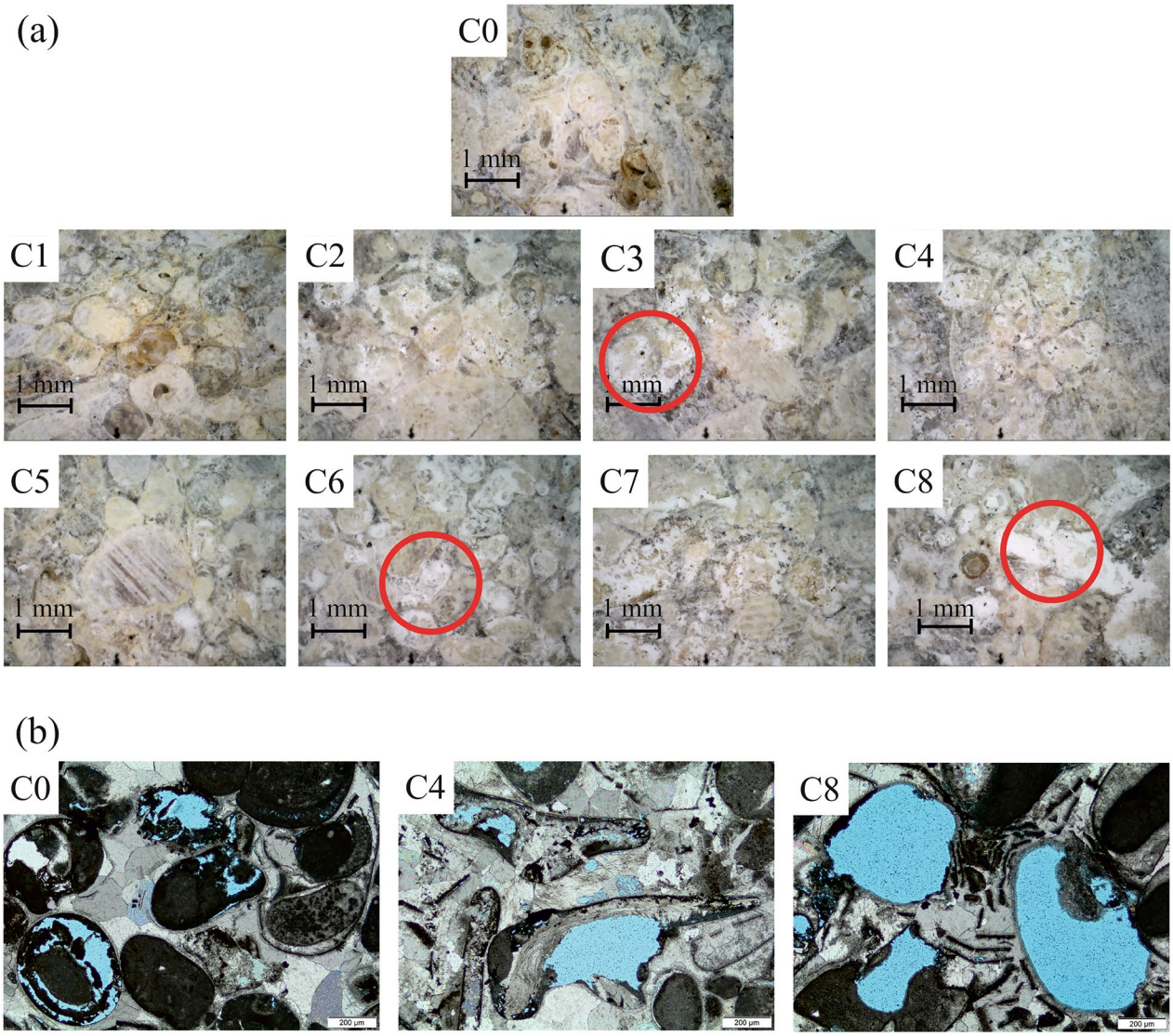

Fig. 4 **a** Optical microscopy results for a control sample (C0), the samples treated with *E5* (C1–C4) and those treated with *E25* (C5–C8) following the 28 day curing period at $T = 20$ °C, % $RH = 75$. The red circles (○) indicate areas of nanolime deposits. **b** Plane polarised light microphotographs of a control (C0), *E5* sample (C4) and *E25* sample (C8) after 28 day curing period at $T = 20$ °C, % $RH = 75$. The samples were impregnated with resin to prevent disintegration and dyed blue to help discriminate pores from the stone matrix

found in *CaLoSiL* are between 50 and 300 nm, and for such small changes in mass as reported in Table 1, would be undetectable under an optical microscope.

Table 1 reports the colorimetric changes of the top and bottom faces of the samples following treatment and carbonation, and the results are displayed in Fig. 5a. The average colour values of 5 control samples (top and bottom faces) were taken as the reference $L^*a^*b^*$ values for Eq. 1. Figure 5a shows good agreement between ΔE^*_{ab} for the top and bottom faces of the treated samples, indicating full immersion has resulted in even treatment to both large surfaces of the sample. The inter-sample variation for the control group is 1.89, indicating that all changes reported in Table 1 are likely the result of treatment. In conservation, colour changes are often assessed in comparison to an observable colour change, the threshold of which for an untrained observer is $\Delta E^*_{ab} > 3.5$ [64]. Using this limit, it can be seen that two *E5* samples (C3 and C4) and three *E25* samples (C6–C8) exhibit observable colour changes. The average ΔE^*_{ab} for

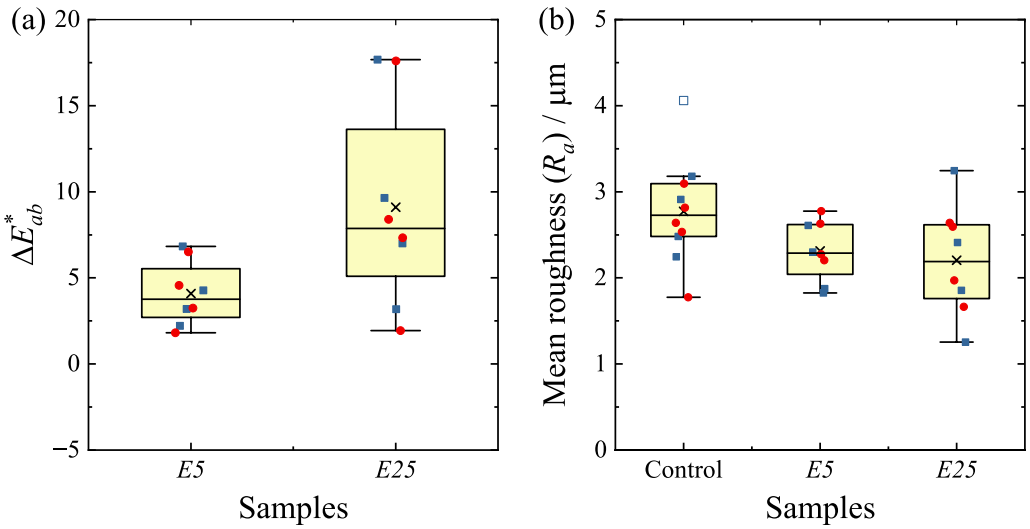

Fig. 5 Box plots showing **a** the global colour change, ΔE^*_{ab}, for samples treated with *E5* and *E25*; **b** the arithmetic average height parameter, R_a, for control samples, *E5* samples and *E25* samples; Measurements from the top face are shown in red circles (●) and the bottom face are shown in blue squares (■), with outliers represented by hollow symbols (○/□). The box represents the interquartile range (25th–75th percentiles) and the whiskers are determined by the 5th and 95th percentiles. The median is represented by the horizontal line while the mean is indicated by ×

samples treated with *E5* is 4.08 ± 1.73, and for *E25* is 9.10 ± 5.48, thus, on average both concentrations result in observable colour changes, with the higher concentration of nanolime (unsurprisingly) resulting in a greater change. Analysis of the ΔL^*, Δa^* and Δb^* values show that the majority of samples experienced an increase in lightness, and a negative shift in Δa^* and Δb^* towards neutral, which can be interpreted as an indication of the commonly reported whitening of samples [3, 21, 32, 46].

The mean surface roughness values, R_a, for the samples are reported in Table 1, and are shown in comparison to the control group in Fig. 5b. The average R_a for the control samples is 2.77 ± 0.58 μm, while for *E5* is 2.31 ± 0.33 μm and *E25* is 2.20 ± 0.59 μm. A two-sample *t*-test on the sample groups was performed to compare the control group and the two treatment groups to determine the probability, *p*, of the likelihood of the null hypothesis explaining the variability. The decrease in mean surface roughness for both the *E5* samples and *E25* samples are approaching significance at the 2σ level in comparison with the control group ($p[E5] = 0.077$; $p[E25] = 0.072$), but are not significantly different from each other ($p = 0.681$). While this suggests that there has been a decrease in surface roughness following treatment, possibly due to accumulation of the nanolime product [26], we note that the resolution of the measurement is limited to 1.5 μm [52], and therefore, we should be cautious not to over-interpret these results.

Sample variation and reproducibility of the drying kinetics

The variation between the drying kinetics of the different samples, before and after treatment, and the reproducibility in the experimental procedure and application method, was assessed using four repeats for each concentration. Figure 6 shows how the drying kinetic parameters changed following treatment with *E5* and *E25* (a full report of the parameters can be found in the Additional file 1: Tables S1 and S2). As expected, despite the same experimental procedure being used for all samples, there is sample variation in the drying kinetics parameters due to natural variation in the pore distributions within samples, which will result in different amounts of water being absorbed, altering the length of phase I (t_c).

The results for the drying kinetics parameters following treatment, for both *E5* and *E25*, show good agreement with the untreated samples in terms of $m_{H_2O}(\infty)$, t_c and D_{II}, and two-sample *t*-tests show that there is no statistically significant change in these quantities ($p[m_{H_2O}(\infty)] = 0.940$; $p[t_c] = 0.642$; $p[D_{II}] = 0.903$). This indicates that although there is some observed surface nanolime deposits (Fig. 4a), it does not contribute significant aggregation or accumulation of nanoparticles capable of blocking pore access. However, Fig. 6c shows there is clear increase in $\dot{m}_{CST}$ following treatment, and a two-sample *t*-test shows that the difference in distributions is approaching significance at the 2σ level ($p[\dot{m}_{CST}] = 0.054$). As stated previously, the phase I rate of evaporation is controlled by the concentration gradient between the surface and the gas above. This increase in $\dot{m}_{CST}$ may be due to subtle

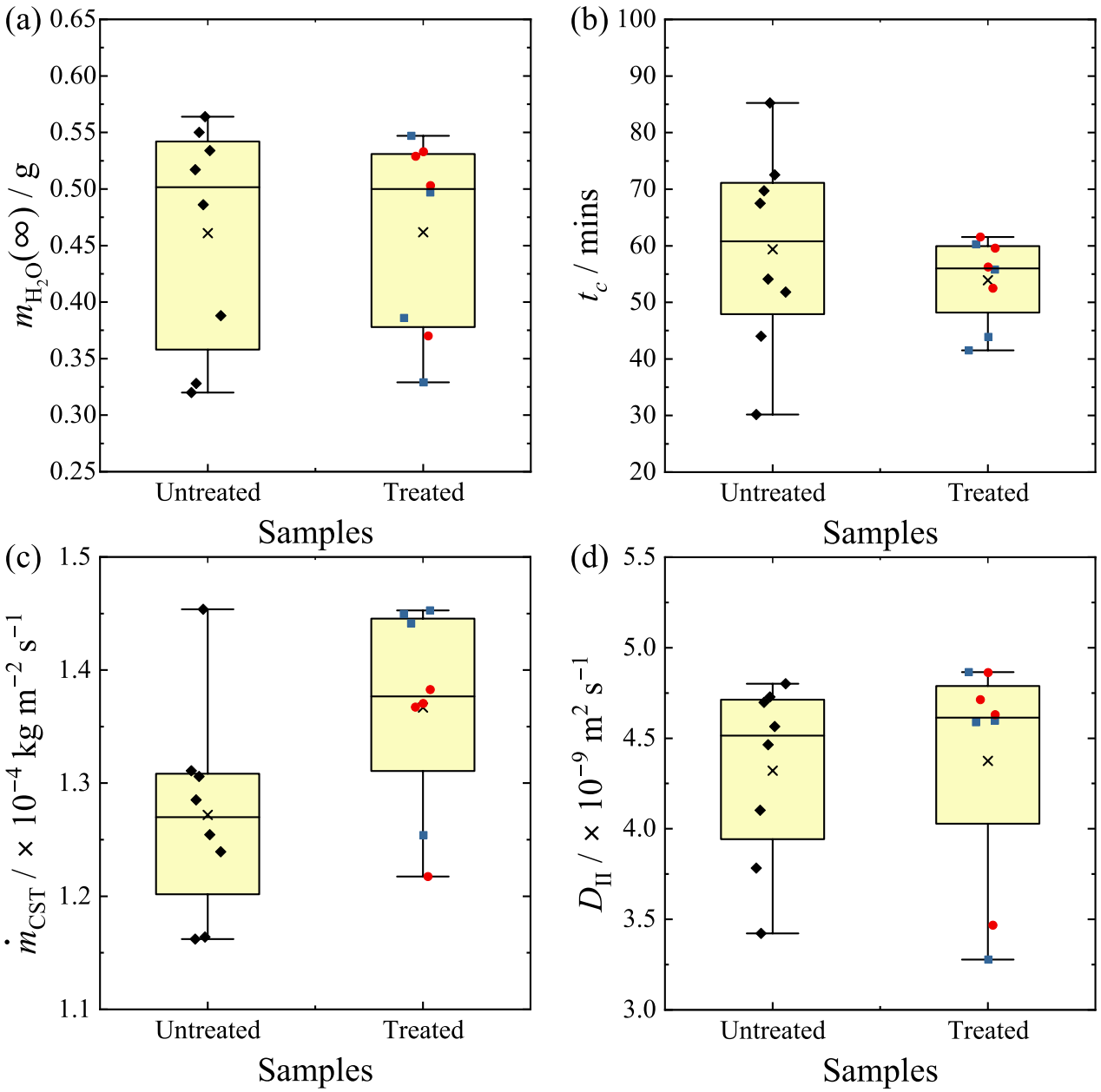

Fig. 6 Box plots showing **a** the mass of water released, $m_{H_2O}(\infty)$, for untreated and treated samples; **b** the critical time, t_c, for untreated and treated samples; **c** the constant mass flux, $\dot{m}_{CST}$, for untreated and treated samples; **d** the phase II diffusivity, D_{II}, for untreated and treated samples; Measurements for untreated samples are shown in black diamonds (♦), samples treated with *E5* are shown in blue squares (■) and samples treated with *E25* are shown in red circles (●). The box represents the interquartile range (25th–75th percentiles) and the whiskers are determined by the 5th and 95th percentiles. The median is represented by the horizontal line while the mean is indicated by ×

changes in the nano- and micro-morphology to which the TRACEiT measurements are not sensitive.

It would be expected that as $m_{H_2O}(\infty)$ remains constant while $\dot{m}_{CST}$ increases, then t_c should decrease. That t_c does not show a significant change may be a result of the subjective nature of its determination and the significant influence that inter- and intra-heterogeneity has on this parameter (i.e., this change to phase II will not occur at the same time throughout the sample). In itself, t_c may be a relatively crude indicator of

changes in the water transport kinetics as the drying process transitions from phase I to phase II.

Despite the variations in the phase I behaviour, the phase II diffusivities are in good agreement pre- and post-treatment. The phase II behaviour, as previously stated, is dominated by vapour transport within the material and is dependent on the internal structure and properties. Thus, these results indicate that there is little-to-no change in the internal surfaces and structure of the stone following treatment that affects vapour transport. One sample, C8, shows a marked increase in Δm_d and ΔE^*_{ab} upon treatment and this is perhaps due to a higher surface deposition compared with the other samples. Despite this, there has been no impact on the ability of this sample to take up water, and its drying kinetics are in line with the other samples. The reasons for this potential deposition are unclear, although we note, visibly this sample seems to possess some large scale (100 μm) surface features (also seen in Fig. 4b) and so may be a morphological outlier, at least compared with the other samples.

Temperature dependence of the drying kinetics

To further investigate if treatment has an impact on the internal surfaces and structure, we investigated the temperature dependence of the drying kinetics pre- and post-treatment to determine the phase II activation energy. The results of this investigation are shown in Fig. 7, and a full report of the parameters is available in the Additional file 1: Tables S3 and S4.

Comparison of Fig. 7a–d, show that there is good agreement between the drying kinetics pre- and post-treatment. As the temperature increases, there is an increase in the rate of evaporation ($\dot{m}_{\mathrm{CST}}$) due to the increase in the concentration gradient between the surface and the environment, and this results in a decrease in the critical time (t_c). Figure 7e and f show plots of $\ln(D_{\mathrm{II}})$ against $1/T$ for samples pre- and post-treatment with *E5* and *E25*, respectively, and the activation energy is determined from the gradient of the linear fits. From Fig. 7e, $E_a(\text{untreated}) = 30.30 \pm 0.60$ kJ mol^{-1} and $E_a(E5) = 30.00 \pm 0.71$ kJ mol^{-1}, and from Fig. 7f $E_a(\text{untreated}) = 30.31 \pm 2.07$ kJ mol^{-1} and $E_a(E25) = 30.77 \pm 1.00$ kJ mol^{-1}. We note that from Fig. 7e and f it can be seen that the phase II diffusivities are in good agreement pre- and post-treatment, as found in the sample variation study. We also note that although the phase II diffusivities are calculated from the gradient of a linear fit using Eq. 7 between 10 and 30 % saturation, good agreement in plots of Eq. 7 is observed to very low water saturation levels ($< 0.01\%$). This result, supported by the sample variation phase II diffusivity measurements, indicates that for Clipsham limestone treated with ethanol dispersed nanolimes by full immersion, independent of the concentration, there is no significant change in the internal surface properties that would lead to different phase II behaviour. This preliminary result is promising as it suggests that the treatment is compatible in terms of water transport kinetics and will not result in trapped moisture and salts, leading to increased weathering. However, further investigation concerning the relationship between consolidation effectiveness and water transport kinetics is required.

Conclusions

In this article, we have investigated the impact of ethanol dispersed nanolime treatments by full immersion at two different concentrations on the drying kinetics of Clipsham limestone, and investigated the variations in these kinetics under different temperatures. We have determined that treatment of the samples did occur as signified by changes in the dry mass and observable colour. This treatment did not result in significant changes in the mass of water released, the time for phase I to end, or the phase II diffusivity, but did result in a small but statistically significant increase to the phase I constant mass flux. Further investigation into the phase II activation energies shows that the post-treatment values are in good agreement with those found pre-treatment, and are in the range previously observed [37, 65, 66].

Further work into the drying kinetics of weathered samples, such as those commonly found in the need of treatment, and investigations into the impact of consolidants on their drying kinetics is required. This work has focused on treatment using ethanol dispersed nanolimes applied by full immersion, however, there are many different application procedures, e.g., brushing, spraying, which may result in different distributions and penetration depths of nanoparticles within the material, and the impact of which on drying kinetics requires further study. Additionally, there are alternative treatments commonly applied in conservation and in retrofitting, for example, water repellent treatments, which are also an area of interest for future investigations. Cavity ring-down spectroscopy can also monitor other species of interest, such as key agents of deterioration e.g., SO_2 or CO_2, allowing investigations into the weathering mechanisms to be carried out.

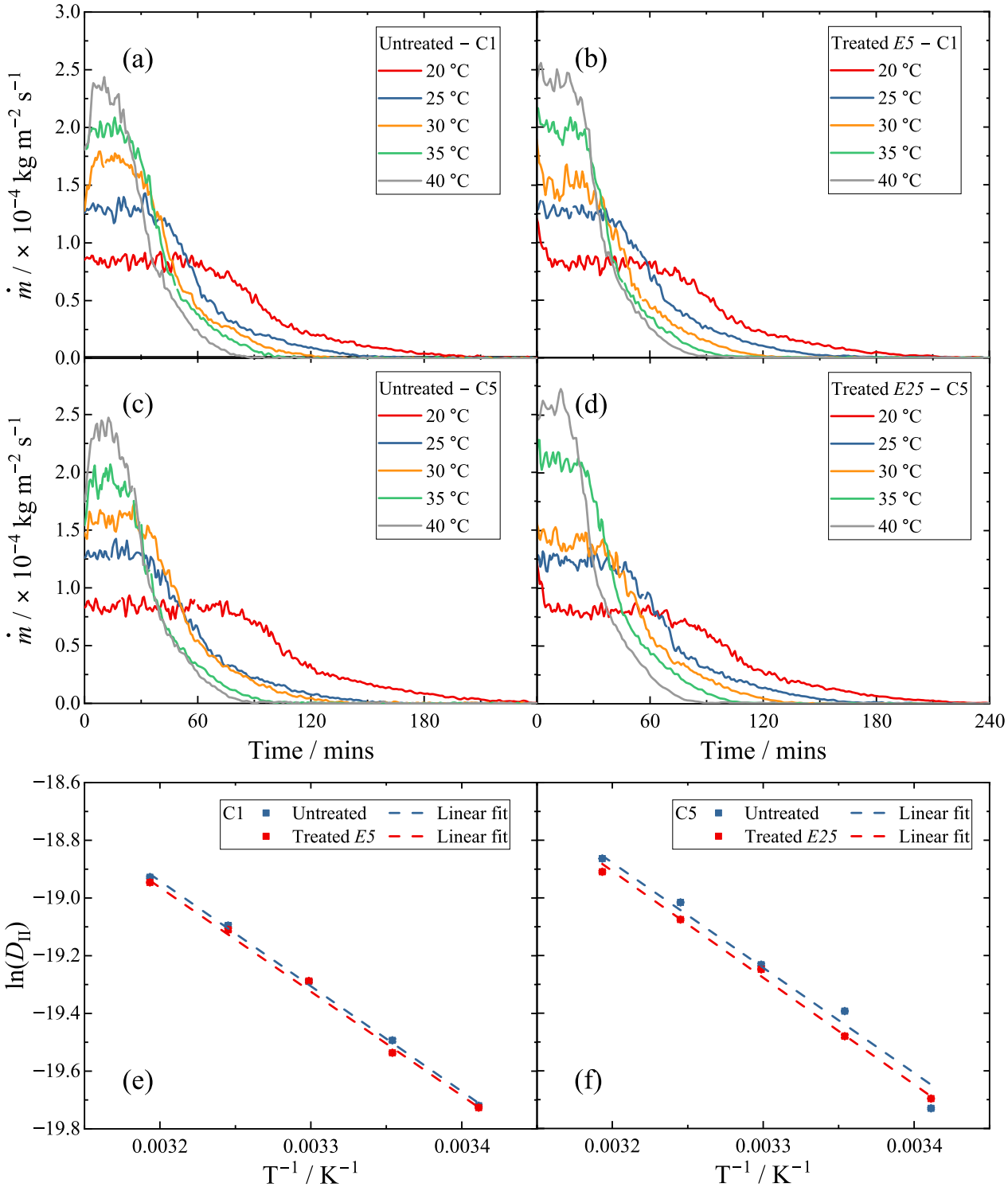

Fig. 7 A plot of the H_2O mass flux, $\dot{m}$, as a function of time with increasing temperature for two Clipsham samples of *ca.* 25 × 25 × 5 mm **a** sample C1 untreated; **b** sample C1 treated with *E5*; **c** sample C5 untreated; **d** sample C5 treated with *E25*. A plot of $\ln(D_{II})$ against $1/T$ based on an Arrhenius relationship between phase II diffusivity and temperature for **e** pre- and post-treatment with *E5*; **f** pre- and post-treatment with *E25*

Abbreviations

AOM	Acousto-optic modulator
amp	Amplifier
CRDS	Cavity ring-down spectroscopy
cw	Continuous wave
IR	Infrared
mfc	Mass flow controller
PC DAQ	Data acquisition system
PD	Photo-detector
RDT	Ring-down time
RH	Relative humidity
slm	Standard litres per minute

Supplementary Information

The online version contains supplementary material available at https://doi.org/10.1186/s40494-023-00938-z.

Additional file 1: **Figure S1**. Scanning electron microscopy images of a control sample, *E5* sample and *E25* sample after 28 day curing period at $T = 20$ °C, % $RH = 75$. **Table S1**. Sample variation, pre- and post-treatment with *E5*. **Table S2**. Sample variation, pre- and post-treatment with *E25*. **Table S3**. Temperature dependence, pre- and post-treatment with *E5*. **Table S4**. Temperature dependence, pre- and post-treatment with *E25*.

Acknowledgements
The authors thank Mrs Hong Zhang (GeoLabs, School of Geography and the Environment, University of Oxford) for her help in preparation of the samples and Dr Jorge Otero (Department of Mineralogy and Petrology, University of Granada) for his guidance in the application of consolidants.

Author contributions
DEB: conceptualization, methodology, validation, formal analysis, investigation, data curation, writing–original draft, writing–review and editing, visualization; RP: conceptualization, methodology, writing–review and editing; GADR: conceptualization, resources, writing–review and editing, supervision; HAV: conceptualization, resources, writing–review and editing, supervision. All authors read and approved the final manuscript.

Funding
This work was supported by the UK Engineering and Physical Sciences Research Council (EPSRC) grant for the Centre for Doctoral Training in Science and Engineering in Arts, Heritage and Archaeology (EP/L016036/1).

Availability of data and materials
The datasets generated during and/or analysed during the current study are available from the corresponding author on reasonable request.

Declarations

Competing interests
The authors declare that they have no competing interests.

Received: 26 January 2023 Accepted: 23 April 2023
Published online: 23 May 2023

References

1. Borsoi G, Lubelli B, van Hees R, Veiga R, Silva AS. Understanding the transport of nanolime consolidants within Maastricht limestone. J Cult Herit. 2016;18:242–9.
2. Doehne E, Price CA. Putting it right: preventive and remedial treatments. In: Doehne E, Price CA, editors. Stone conservation: an overview of current research. Research in conservation. 2nd ed. Los Angeles: Getty Conservation Institute; 2010. p. 27–48.
3. Otero J, Starinieri V, Charola AE. Influence of substrate pore structure and nanolime particle size on the effectiveness of nanolime treatments. Constr Build Mater. 2019;209:701–8.
4. Rodriguez-Navarro C, Ruiz-Agudo E. Nanolimes: from synthesis to application. Pure Appl Chem. 2018;90:523–50.
5. Pozo-Antonio JS, Otero J, Alonso P, Mas i Barberà X,. Nanolime- and nanosilica-based consolidants applied on heated granite and limestone: effectiveness and durability. Constr Build Mater. 2019;201:852–70.
6. Giorgi R, Dei L, Baglioni P. A new method for consolidating wall paintings based on dispersions of lime in alcohol. Stud Conserv. 2000;45:154–61.
7. Zhu J, Zhang P, Ding J, Dong Y, Cao Y, Dong W, et al. Nano $Ca(OH)_2$: a review on synthesis, properties and applications. J Cult Herit. 2021;50:25–42.
8. Daniele V, Taglieri G, Quaresima R. The nanolimes in cultural heritage conservation: characterisation and analysis of the carbonation process. J Cult Herit. 2008;9:294–301.
9. Rodriguez-Navarro C, Suzuki A, Ruiz-Agudo E. Alcohol dispersions of calcium hydroxide nanoparticles for stone conservation. Langmuir. 2013;29:11457–70.
10. Rodriguez-Navarro C, Vettori I, Ruiz-Agudo E. Kinetics and mechanism of calcium hydroxide conversion into calcium alkoxides: implications in heritage conservation using nanolimes. Langmuir. 2016;32:5183–94.
11. Camerini R, Poggi G, Chelazzi D, Ridi F, Giorgi R, Baglioni P. The carbonation kinetics of calcium hydroxide nanoparticles: a boundary nucleation and growth description. J Colloid Interface Sci. 2019;547:370–81.
12. Nuño M, Pesce GL, Bowen CR, Xenophontos P, Ball RJ. Environmental performance of nano-structured $Ca(OH)_2/TiO_2$ photocatalytic coatings for buildings. Build Environ. 2015;92:734–42.
13. Samanta A, Chanda DK, Das P, Ghosh J, Mukhopadhyay A, Dey A. Synthesis of nano calcium hydroxide in aqueous medium. J Am Ceram Soc. 2016;99:787–95.
14. Taglieri G, Daniele V, Macera L, Mondelli C. Nano $Ca(OH)_2$ synthesis using a cost-effective and innovative method: reactivity study. J Am Ceram Soc. 2017;100:5766–78.
15. Martínez-Ramírez S, Higueruela LR, Cascales I, Martín-Garrido M, Blaco-Varela MT. New approach to nanolime synthesis at ambient temperature. SN Appl Sci. 2019;1:105.
16. Ševčík R, Viani A, Machová D, Lanzafame G, Mancini L, Appavou MS. Synthetic calcium carbonate improves the effectiveness of treatments with nanolime to contrast decay in highly porous limestone. Sci Rep. 2019;9:15278.
17. D'Armada P, Hirst E. Nano-lime for consolidation of plaster and stone. J Archit Conserv. 2012;18:63–80.
18. Licchelli M, Malagodi M, Weththimuni M, Zanchi C. Nanolimes for conservation of bio-calcarenite stone. Appl Phys A Mater Sci Process. 2014;114:673–83.
19. Daniele V, Taglieri G, Macera L, Rosatelli G, Otero J, Charola AE. Green approach for an eco-compatible consolidation of the Agrigento biocalcarenites surface. Constr Build Mater. 2018;186:1188–99.
20. Tzavellos S, Pesce GL, Wu Y, Henry A, Robson S, Ball RJ. Effectiveness of nanolime as a stone consolidant: a 4-year study of six common UK limestones. Materials. 2019;12:2673.
21. Gherardi F, Otero J, Blakeley R, Colston B. Application of nanolimes for the consolidation of limestone from the medieval Bishop's palace, Lincoln. UK Stud Conserv. 2020;65(sup1):P90–7.
22. Otero J, Starinieri V, Charola AE, Taglieri G. Influence of different types of solvent on the effectiveness of nanolime treatments on highly porous mortar substrates. Constr Build Mater. 2020;230: 117112.
23. Macera L, Daniele V, Duchetta F, Casciardi S, Taglieri G. New nanolimes for eco-friendly and customized treatments to preserve the biocalcarenites of the "Valley of Temples" of Agrigento. Constr Build Mater. 2021;306: 124811.
24. Otero J, Charola AE, Starinieri V. Preliminary investigations of compatible nanolime treatments on Indiana limestone and weathered marble stone. Int J Archit Herit. 2022;16:394–404.

25. Elert K, Jroundi F, Benavides-Reyes C, Correa Gómez E, Gulotta D, Rodriguez-Navarro C. Consolidation of clay-rich earthen building materials: a comparative study at the Alhambra fortress (Spain). J Build Eng. 2022;50: 104081.
26. López-Arce P, Gomez-Villalba LS, Pinho L, Fernández-Valle ME, Álvarez de Buergo M, Fort R. Influence of porosity and relative humidity on consolidation of dolostone with calcium hydroxide nanoparticles: effectiveness assessment with non-destructive techniques. Mater Character. 2010;61:168–84.
27. Ruffolo SA, La Russa MF, Aloise P, Belfiore CM, Macchia A, Pezzino A, et al. Efficacy of nanolime in restoration procedures of salt weathered limestone rock. Appl Phys A Mater Sci Process. 2014;114:753–8.
28. Zornoza-Indart A, López-Arce P, Gomez-Villalba L, Varas-Muriel M, Fort R. Consolidation of deteriorated carbonate stones with $Ca(OH)_2$ nanoparticles. In: Proceedings of the 12th International Conference on the deterioration and conservation of stone. 2012.
29. Arizzi A, Gomez-Villalba LS, Lopez-Arce P, Cultrone G, Fort R. Lime mortar consolidation with nanostructured calcium hydroxide dispersions: the efficacy of different consolidating products for heritage conservation. Eur J Miner. 2015;27:311–23.
30. Niedoba K, Slížková Z, Frankeová D, Nunes CL, Jandejsek I. Modifying the consolidation depth of nanolime on Maastricht limestone. Constr Build Mater. 2017;133:51–6.
31. Otero J, Pozo-Antonio JS, Montojo C. Influence of application method and number of applications of nanolime on the effectiveness of the Doulting limestone treatments. Mater Struct. 2021;54:41.
32. Pozo-Antonio JS, Otero J, González N. The influence of using wet cellulose poultice on nanolime consolidaton treatments applied on a limestone. Constr Build Mater. 2022;337: 127615.
33. Borsoi G, Lubelli B, van Hees R, Veiga R, Silva AS. Evaluation of the effectiveness and compatibility of nanolime consolidants with improved properties. Constr Build Mater. 2017;142:385–94.
34. Taglieri G, Otero J, Daniele V, Gioia G, Macera L, Starinieri V, et al. The biocalcarenite stone of Agrigento (Italy): preliminary investigations of compatible nanolime treatments. J Cult Herit. 2018;30:92–9.
35. Becerra J, Ortiz P, Martín JM, Zaderenko AP. Nanolimes doped with quantum dots for stone consolidation assessment. Const Build Mater. 2019;199:581–93.
36. Browne DE, Peverall R, Ritchie GAD, Viles HA. Determining water transport kinetics in limestone by dual-wavelength cavity ring-down spectroscopy. Anal Chem. 2022;94:3126–34.
37. Browne DE, Peverall R, Ritchie GAD, Viles HA. Direct monitoring of drying kinetics of building limestones using cavity ring-down spectroscopy. Constr Build Mater. 2023;369: 130554.
38. Scherer GW. Theory of drying. J Am Ceram Soc. 1990;73:3–14.
39. Hall C, Hoff WD. Evaporation and drying. In: Hall C, Hoff WD, editors. Water transport in brick, stone and concrete. 3rd ed. London: CRC Press; 2021. p. 239–261.
40. Meyer DE, Hackerman N. Adsorption thermodynamics of the interaction of water and various silica powders. J Phys Chem. 1966;70:2077–86.
41. Salter HE, Lobel MD. The University Press and other modern buildings. In: Salter HE, editor. A history of the county of Oxford. 3rd ed. London: The University of Oxford; 1954.
42. Schaffer RJ II. The weathering, preservation and restoration of stone buildings. J R Soc Arts. 1955;103:843–67.
43. Tyack G. From modernism to post-modernism. In: Tyack G, editor. An architectural guide. Oxford: Oxford University Press; 1998.
44. Ashton M. The stratigraphy of the Lincolnshire Limestone Formation (Bajocian) in Linconshire and Rutland (Leicestershire). Proc Geol Assoc. 1980;91:203–23.
45. Emery D, Dickson JA. A syndepositional meteoric phreatic lens in the Middle Jurassic Lincolnshire Limestone, England, U.K. Sediment Geol. 1989;65:273–84.
46. Borsoi G, Lubelli B, van Hees R, Veiga R, Silva AS. Optimization of nanolime solvent for the consolidation of coarse porous limestone. Appl Phys A Mater Sci Process. 2016;122:846.
47. Borsoi G, Lubelli B, van Hees R, Veiga R, Silva AS, Colla L, et al. Effect of solvent on nanolime transport within limestone: how to improve in-depth deposition. Colloids Surf A. 2016;497:171–81.
48. Rodriguez-Navarro C, Elert K, Ševčík R. Amorphous and crystalline calcium carbonate phases during carbonation of nanolimes: implications in heritage conservation. CrystEngComm. 2016;18:6594–607.
49. Ziegenbalg G, Dietze C, Ziegenbalg G. Fundamentals of Nanolime. In: Ziegenbalg G, Drd, Dietze C, Schuch D, editors. Nanomaterials architecture and art conservation. Pan Stanford; New york; 2018. p. 131–165.
50. Odgers D. Nanolime: a practical guide to its use for consolidating weathered limestone. England: Historic England; 2017.
51. ISO/CIE 11664-4:2019(E). Colorimetry - Part 4: CIE 1976 L*a*b* colour space. International Organization for Standardization; 2019.
52. INNOWEP. TRACEiT® User Manual. INNOWEP GmbH; 2015.
53. Gadelmawla ES, Koura MM, Maksoud TMA, Elewa IM, Soliman HH. Roughness parameters. J Mater Process Technol. 2002;123:133–45.
54. BS EN 12407:2007. Natural stone test methods – petrographic examination. British Standards Institution; 2007.
55. O'Keefe A, Deacon DAG. Cavity ring-down optical spectrometer for absorption measurements using pulsed laser sources. Rev Sci Instrum. 1988;59:2544–51.
56. Romanini D, Kachanov AA, Stoeckel F. Diode laser cavity ring down spectroscopy. Chem Phys Lett. 1997;270:538–45.
57. Wheeler MD, Newman SM, Orr-Ewing AJ, Ashfold MNR. Cavity ring-down spectroscopy. J Chem Soc Faraday Trans. 1998;94:337–51.
58. Berden G, Peeters R, Meijer G. Cavity ring-down spectroscopy: experimental schemes and applications. Int Rev Phys Chem. 2000;19:565–607.
59. Mazurenka M, Orr-Ewing AJ, Peverall R, Ritchie GAD. Cavity ring-down and cavity enhanced spectroscopy using diode lasers. Annu Rep Prog Chem Sect C Phys Chem. 2005;101:100–42.
60. Gordon IE, Rothman LS, Hargreaves RJ, Hashemi R, Karlovets EV, Skinner FM, et al. The HITRAN2020 molecular spectroscopic database. J Quant Spectrosc Radiat Transf. 2022;277: 107949.
61. Crank J. Diffusion in a plane sheet. In: Crank J, editor. The mathematics of diffusion. 2nd ed. Oxford: Oxford University Press; 1975. p. 44–68
62. Bakhshi M, Mobasher B. Experimental observations of early-age drying of Portland cement paste under low-pressure conditions. Cem Concr Compos. 2011;33:474–84.
63. Kaszowska Z, Malek K, Staniszewska-Slezak E, Niedzielska K. Raman scattering or fluorescence emission? Raman spectroscopy study on lime-based building and conservation materials. Spectrochim Acta Part A. 2016;169:7–15.
64. Mokrzycki WS, Tatol M. Colour Difference ΔE – a survey. Mach Graph Vis. 2011;20:383–411.
65. Fiorentini C, Demarchi SM, Quintero Ruiz NA, Martín Torrez Irigoyen R, Giner SA. Arrhenius activation energy for water diffusion during drying of tomato leathers: the concept of characteristic product temperature. Biosyst Eng. 2015;132:39–46.
66. Gualtieri AF, Ricchi A, Lassinantti Gualtieri M, Maretti S, Tamburini M. Kinetic study of the drying process of clay bricks. J Therm Anal Calorim. 2016;123:153–67.

Publisher's Note